Electronic Supplementary Information

Efficient Solar-Driven Hydrogen Peroxide Production Enabled by Perovskite Electrochemical Device Integrated with a Cobalt-Based Chiral Catalyst

Young Sun Park[1‡], Jaerim Kim[2,3‡], Subin Moon[1‡], Eunji Ahn[2,4], Hyeonwoong Hwang[2], Sang-Hoon You[2], Juwon Lee[5], Chang-Seop Jeong[1], Wooyong Jeong[1], Hyoung-il Kim[5], Yong-Tae Kim[2], Kug-Seung Lee[6], Donghwa Le [2,4], Jong Kyu Kim[2*], and Jooho Moon[1*]

[1] Department of Materials Science and Engineering, Yonsei University, Seoul 03722, Republic of Korea

[2] Department of Materials Science and Engineering, Pohang University of Science and Technology (POSTECH), 77 Cheongam-Ro, Nam-Gu, Pohang 37673, Republic of Korea

[3]Department of Chemistry, Northwestern University, 2145 Sheridan Road, Evanston, IL 60208, USA.

[4]Division of Advanced Materials Science, Pohang University of Science and Technology (POSTECH), 77 Cheongam-Ro, Nam-Gu, Pohang 37673, Republic of Korea

[5]Department of Civil & Environmental Engineering, Yonsei University, 50 Yonsei-ro Seodaemun-gu, Seoul 03722, Republic of Korea

[6]Pohang Accelerator Laboratory, Pohang University of Science and Technology, Pohang 37673, Republic of Korea

[*]Correspondence: kimjk@postech.ac.kr, jmoon@yonsei.ac.kr

‡ These authors contributed equally.

Keywords: oxygen reduction reaction, hydrogen peroxide production, chiral catalyst, chirality-induced spin selectivity, spin polarization, photosynthesis

Supplementary Figures

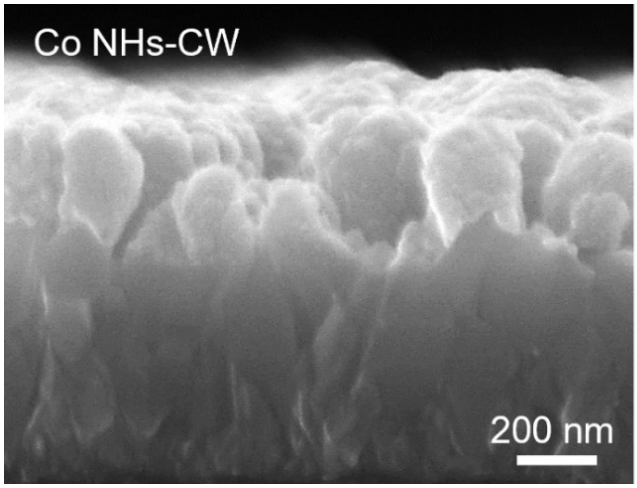

Fig. S1 Cross-sectional SEM image of Co NHs-CW on FTO.

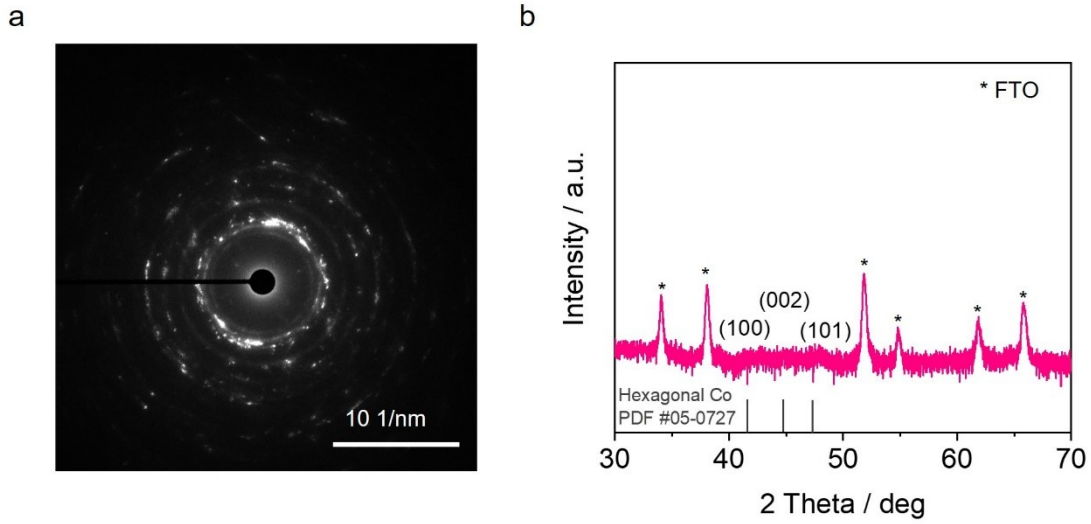

Fig. S2 a) SAED and b) XRD patterns of Co NHs-CW catalyst.

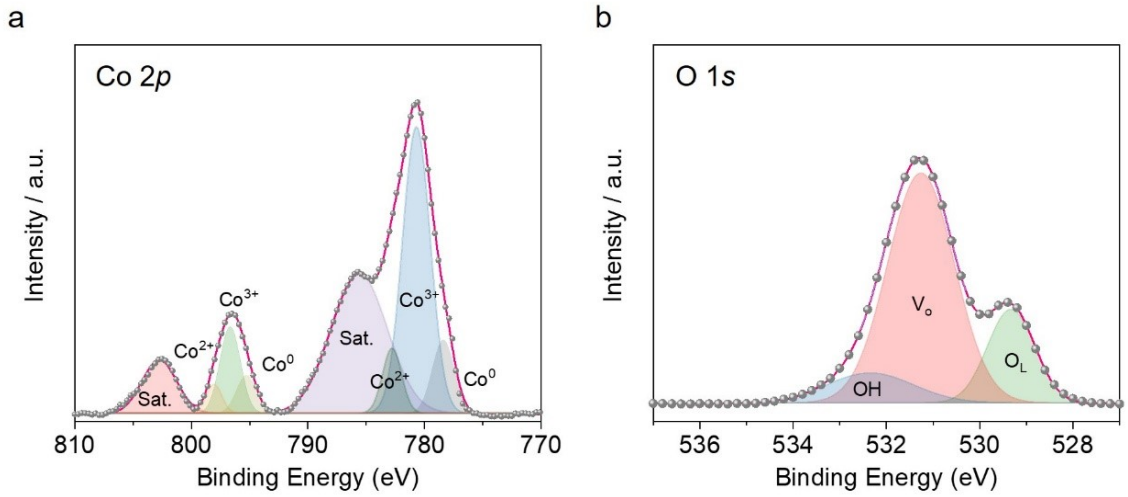

Fig. S3 High-resolution XPS spectra of Co NHs-CW: deconvolutions of a) Co 2*p* and b) O 1*s* regions.

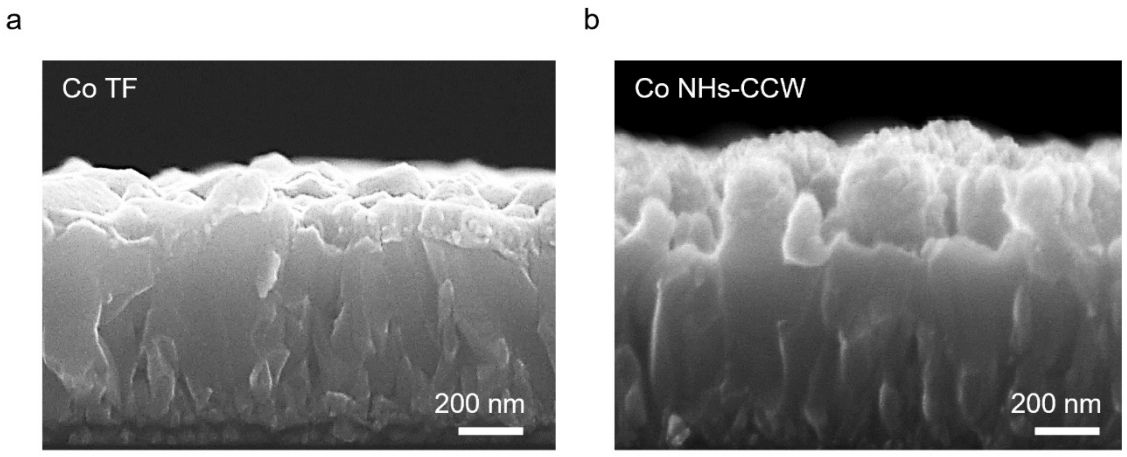

Fig. S4 Cross-sectional SEM images of a) Co TF and b) Co CCW.

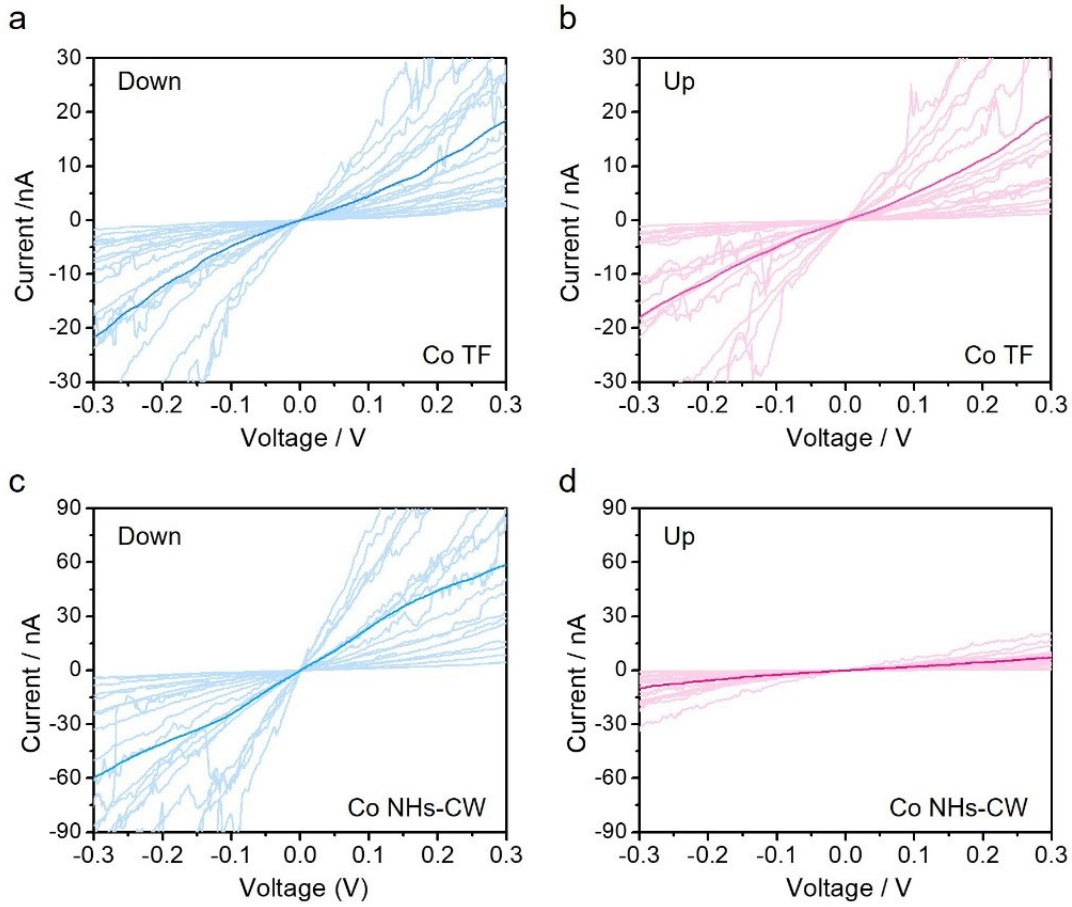

Fig. S5 Raw data for *I–V* curves obtained from mCP-AFM analysis with a pre-magnetized tip aligned along the upward or downward magnetic field orientations at different positions: a, b) Co TF and c, d) Co NHs-CW.

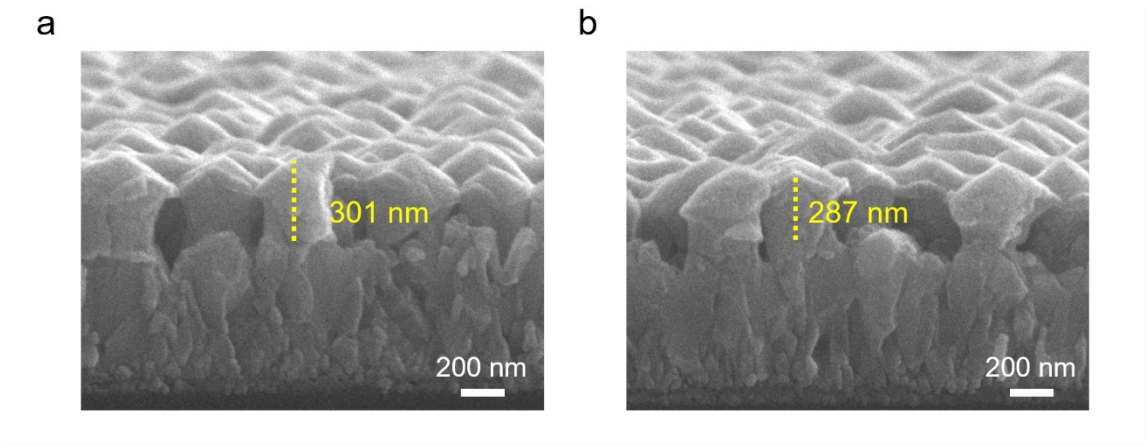

Fig. S6 Cross-sectional SEM images of a) Co NHs-CW 10, and b) Co NHs-CW 15.

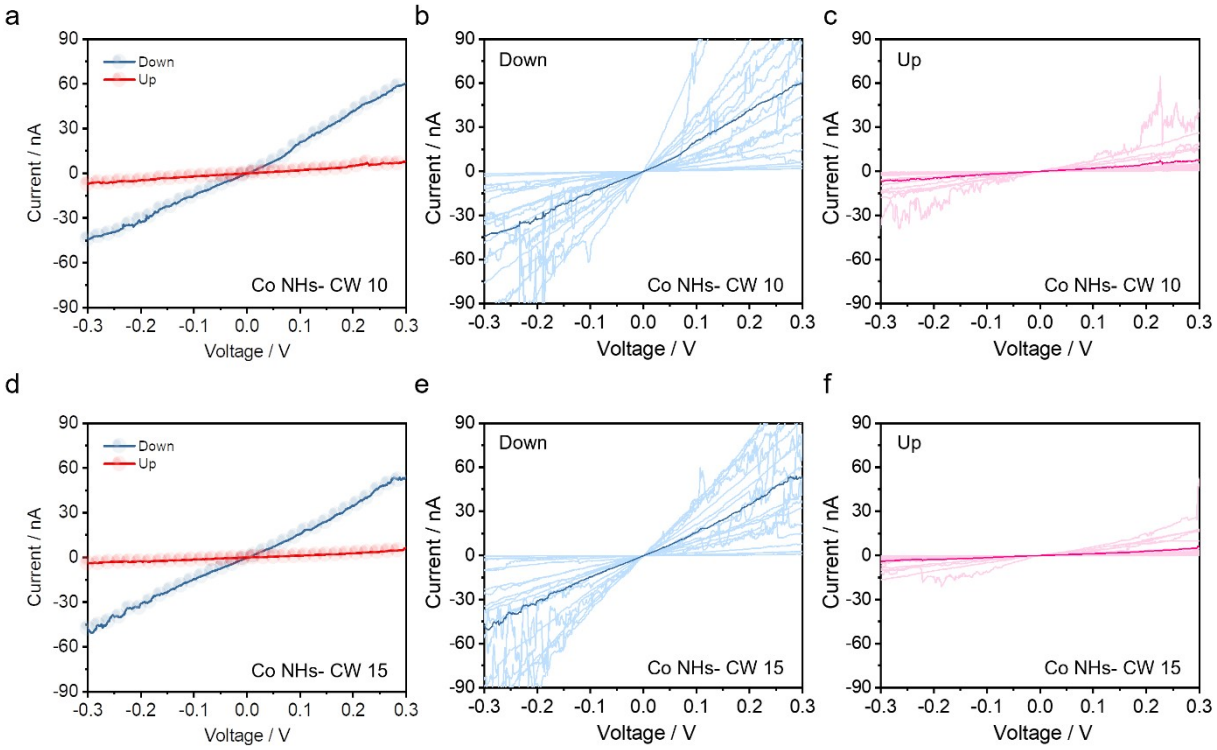

Fig. S7 a),d) Average results and b), c), e), f) raw data for $I-V$ curves obtained from mCP-AFM measurements with a pre-magnetized tip aligned along the upward or downward magnetic field orientations at different positions on Co NHs-CW 10 and 15.

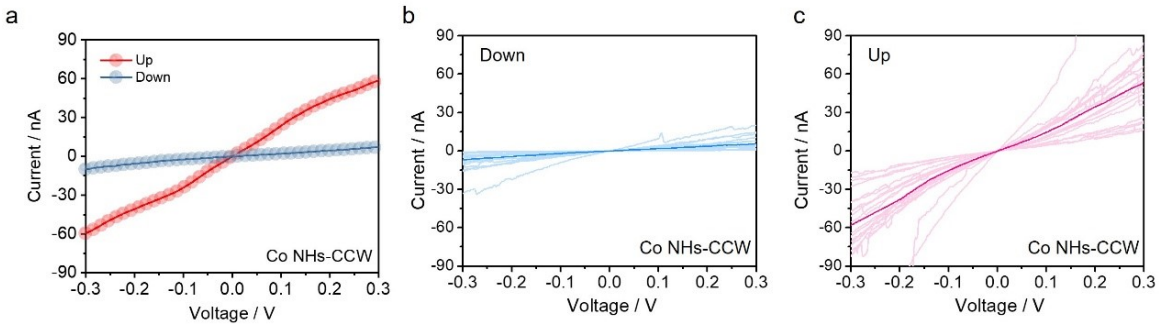

Fig. S8 a) Average results and b, c) raw data for *I–V* curves obtained from mCP-AFM measurements with a pre-magnetized tip aligned along the upward or downward magnetic field orientations at different positions on Co NHs-CCW.

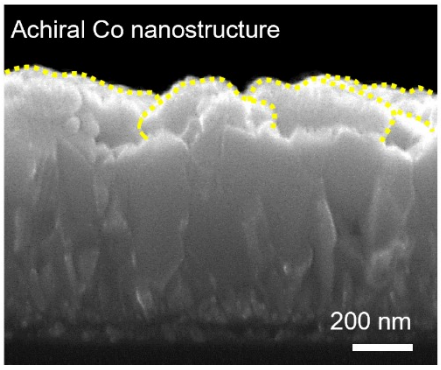

Fig. S9 Cross-sectional image of Co achiral nanostructure.

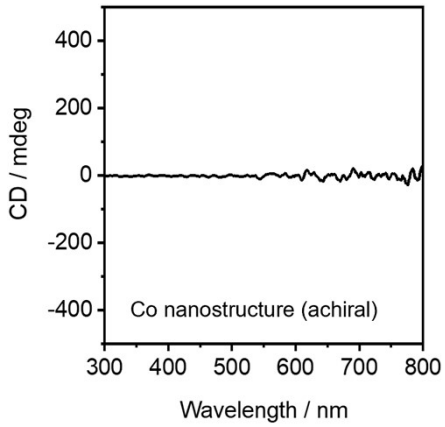

Fig. S10 CD spectra of achiral Co nanostructure.

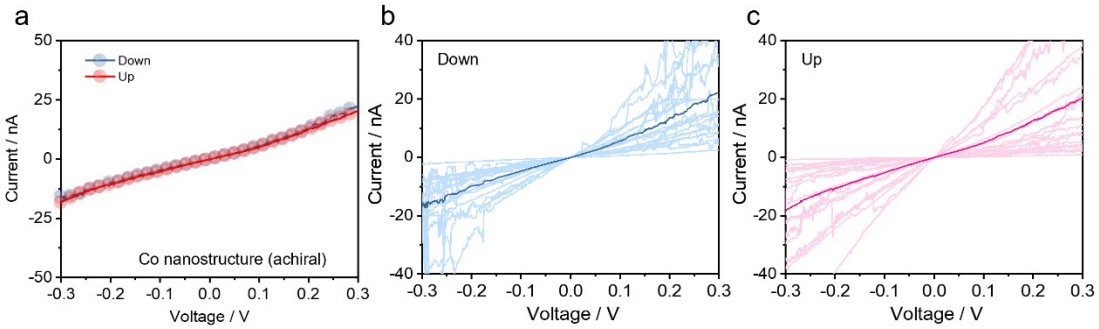

Fig. S11 a) Average results and b), c) raw data for $I-V$ curves obtained from mCP-AFM measurements with a pre-magnetized tip aligned along the upward or downward magnetic field orientations at different positions on the achiral Co nanostructure.

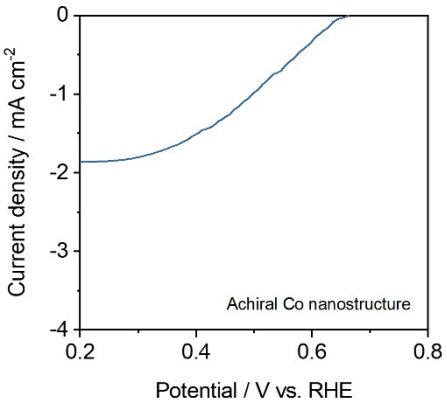

Fig. S12 LSV curve of achiral Co nanostructure in O_2-saturated 0.1 M KOH.

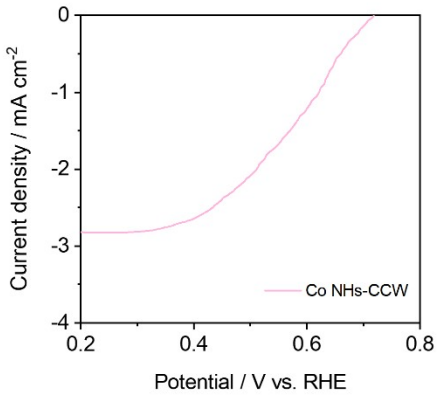

Fig. S13 LSV curve of Co NHs-CCW in O_2-saturated 0.1 M KOH.

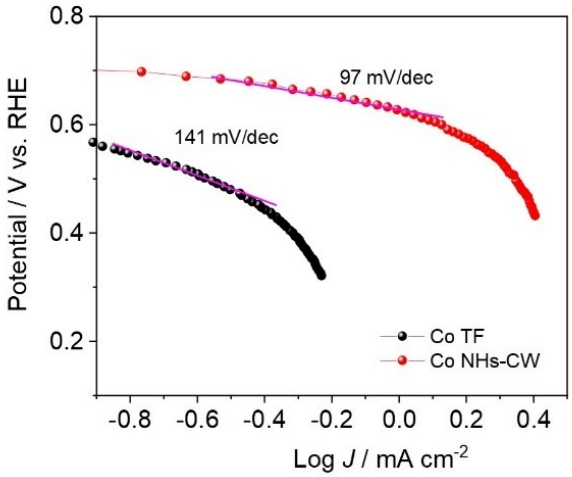

Fig. S14 Tafel slopes of Co NHs-CW and TF in the $2e^-$ ORR process.

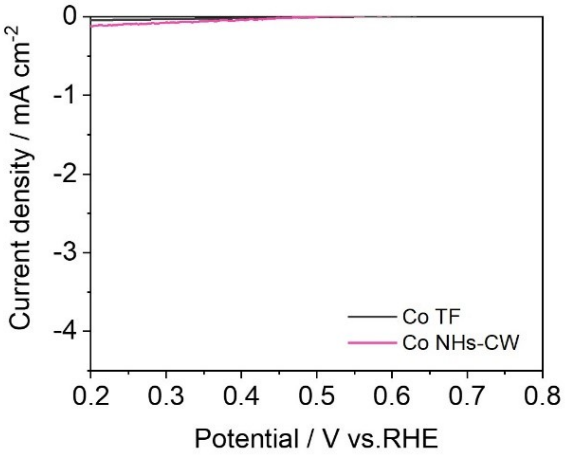

Fig. S15 LSV curves of Co NHs-CW and Co TF, measured in Ar-saturated 0.1 M KOH in the absence of oxygen.

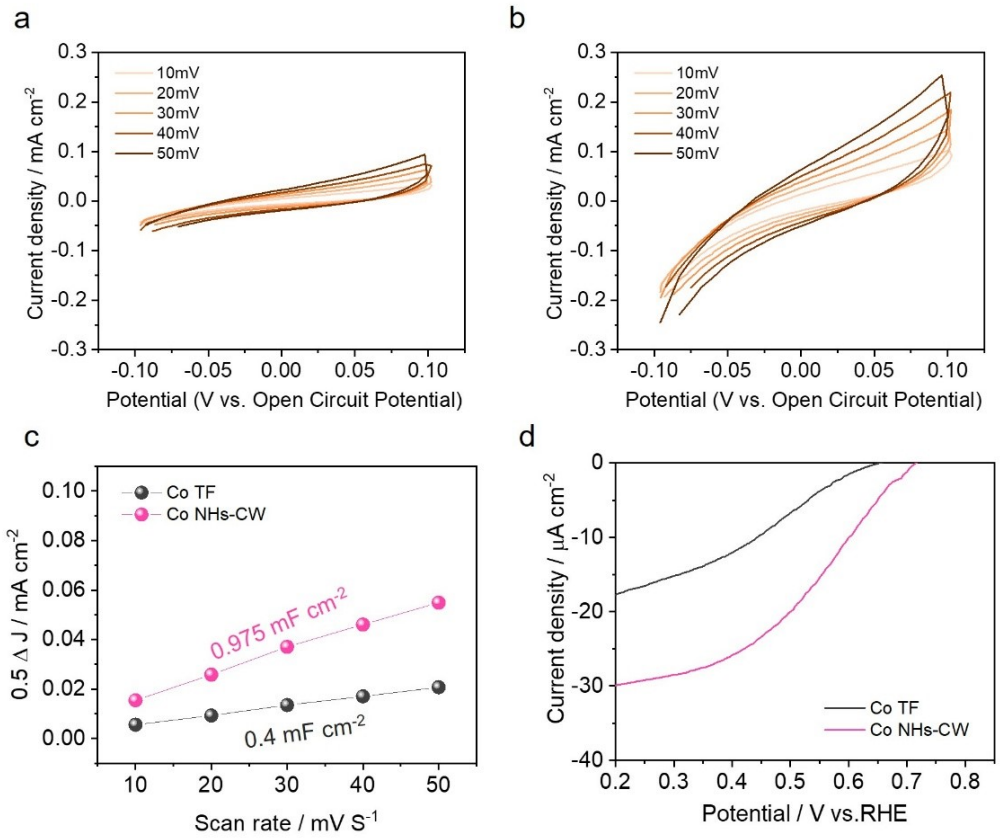

Fig. S16 CV curves for a) Co NHs-CW and b) Co TF in O_2-saturated 0.1 M KOH. c) Capacitive current densities of Co NHs-CW and Co TF as a function of scan rate. d) LSV curves for Co NHs-CW and Co TF in O_2-saturated 0.1 M KOH, based on ECSA-normalized current densities.

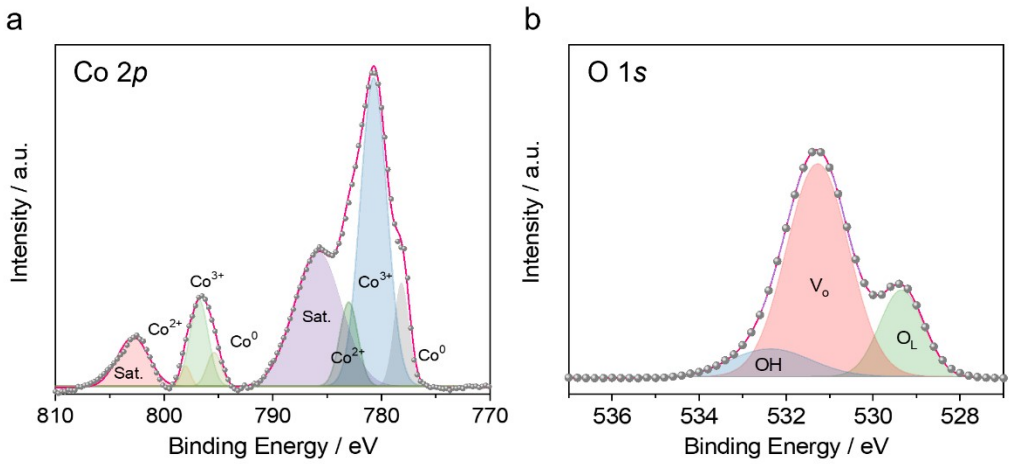

Fig. S17 XPS spectra of a) Co 2*p* and b) O 1*s* for Co TF.

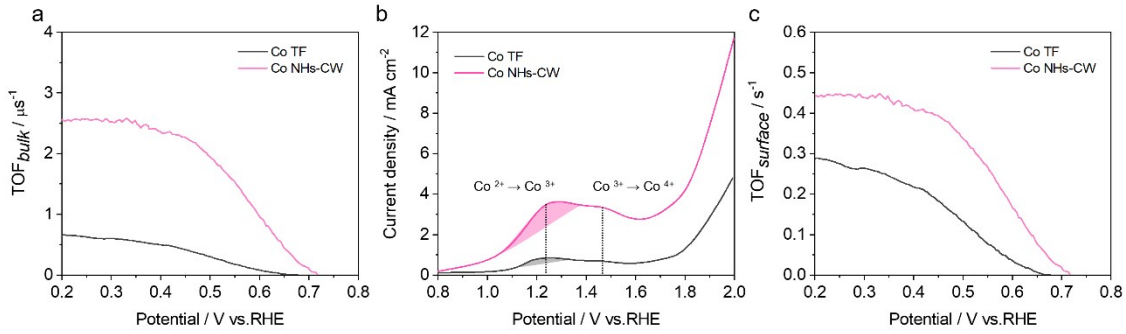

Fig. S18 a) Bulk TOF of Co TF and Co NHs-CW catalysts. b) CV measurement obtained in Ar-saturated 0.1 M KOH showing the characteristic Co redox transitions, and c) surface TOF derived from the integrated area of the oxidation peak for Co TF and Co NHs-CW catalysts.

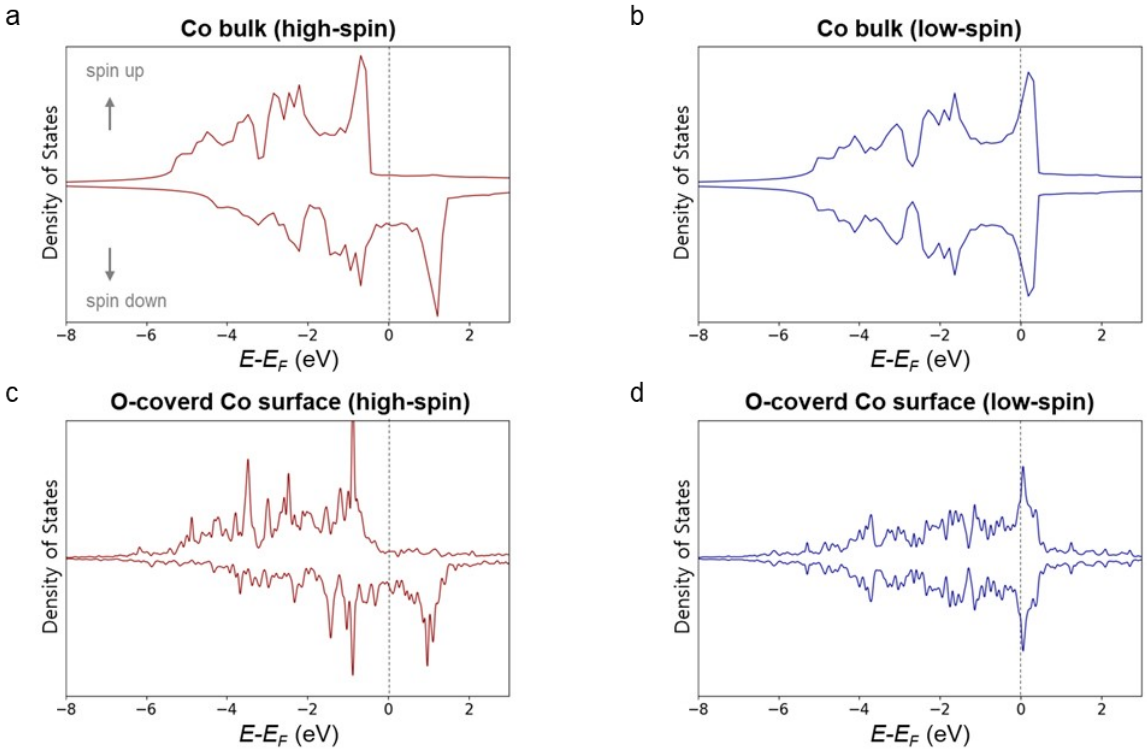

Fig. S19 Spin-polarized density of states (DOS) for cobalt in in different electronic conFig. urations: a) bulk Co in high-spin state, b) bulk Co in low-spin state, c) Co atoms on O-covered Co(002) surface in high-spin state, and d) Co atoms on O-covered Co(002) surface in low-spin state.

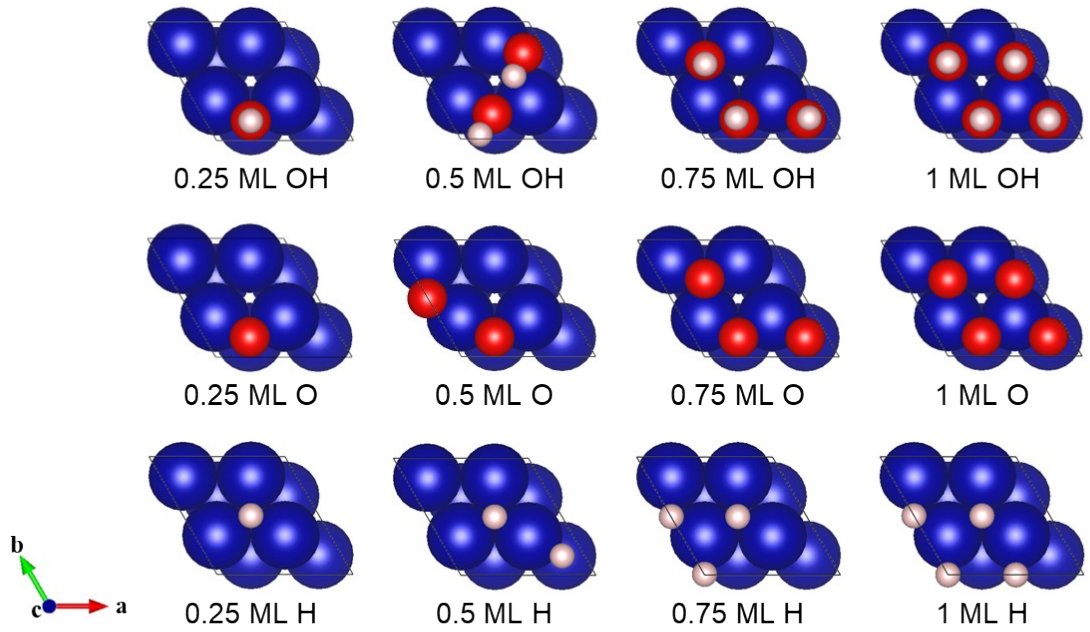

Fig. S20 Top views of adsorbate-covered Co(002) surfaces modeled using a p(2×2) supercell. Studied conFig. urations include 0.25, 0.5, 0.75, and 1 ML coverages of O, OH, and H species. Blue, red, and light pink spheres represent Co, O, and H atoms, respectively.

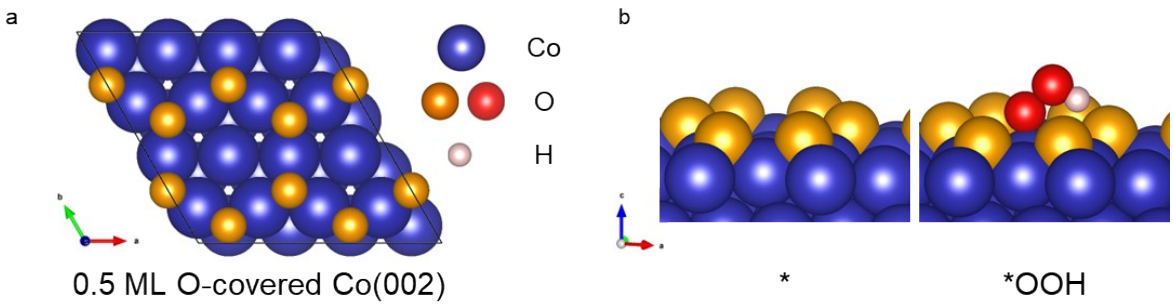

Fig. S21 a) Top view of the 0.5 ML O-covered Co(002) surface. b) Relaxed structures of the active site (*) and *OOH adsorbate.

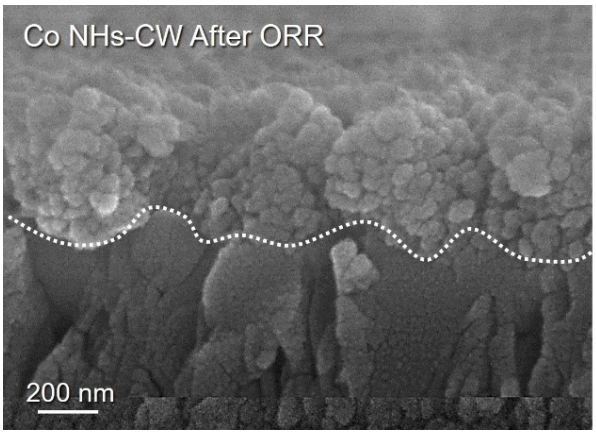

Fig. S22 Cross-sectional SEM images of Co NHs-CW after long-term stability test.

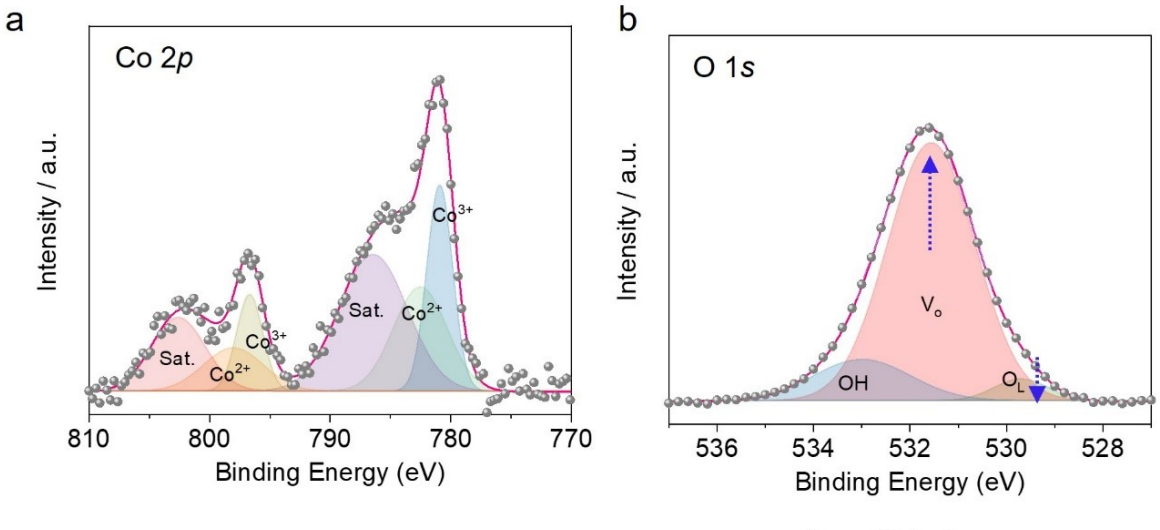

Fig. S23 High-resolution XPS spectra of Co NHs-CW after long-term stability test: deconvolutions of a) Co 2*p* and b) O 1*s* regions.

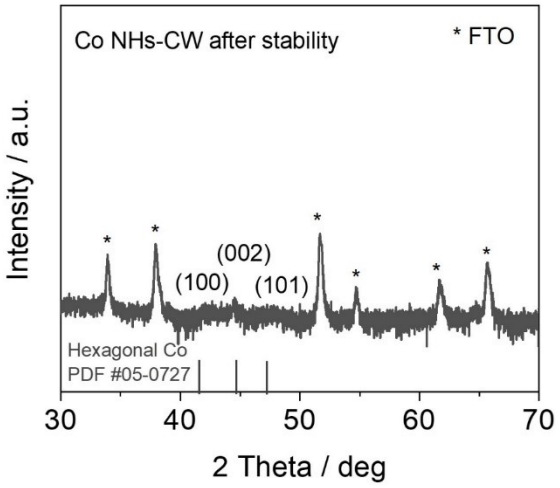

Fig. S24 XRD patterns of Co NHs-CW after long-term stability test.

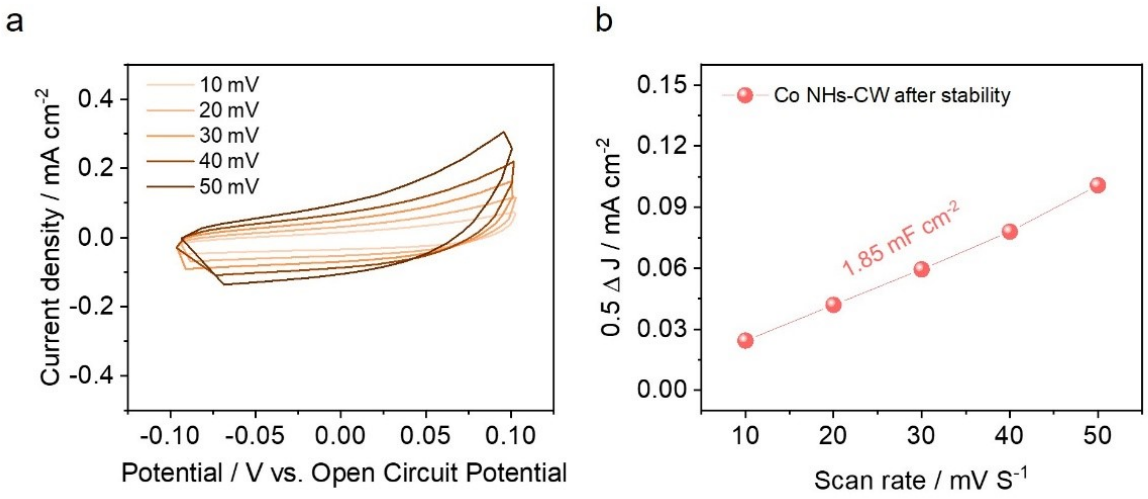

Fig. S25 a) CV curves for Co NHs-CW after long-term stability test in O_2-saturated 0.1 M KOH. b) Capacitive current density of Co NHs-CW after long-term stability test as a function of scan rate.

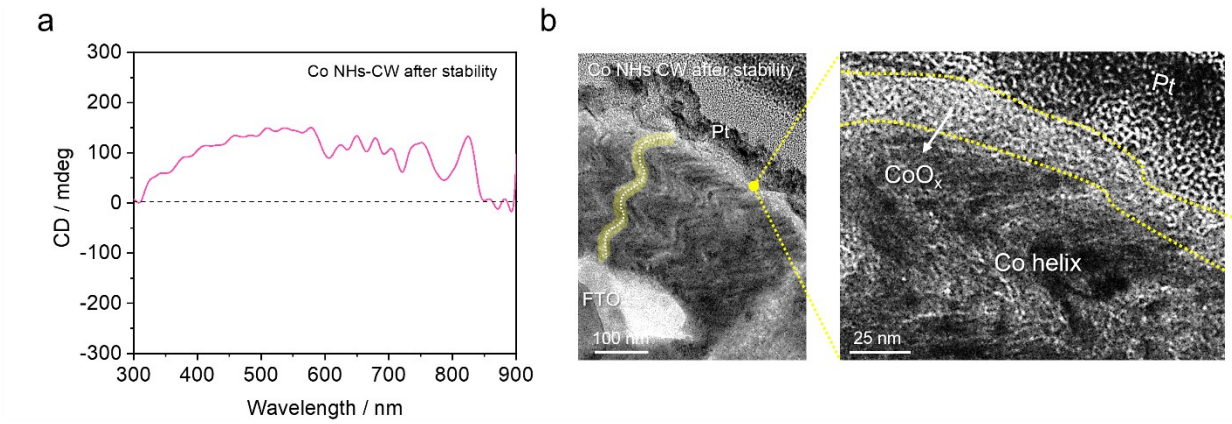

Fig. S26 a) CD spectrum and b) cross-sectional TEM image of Co NHs-CW after long-term stability test.

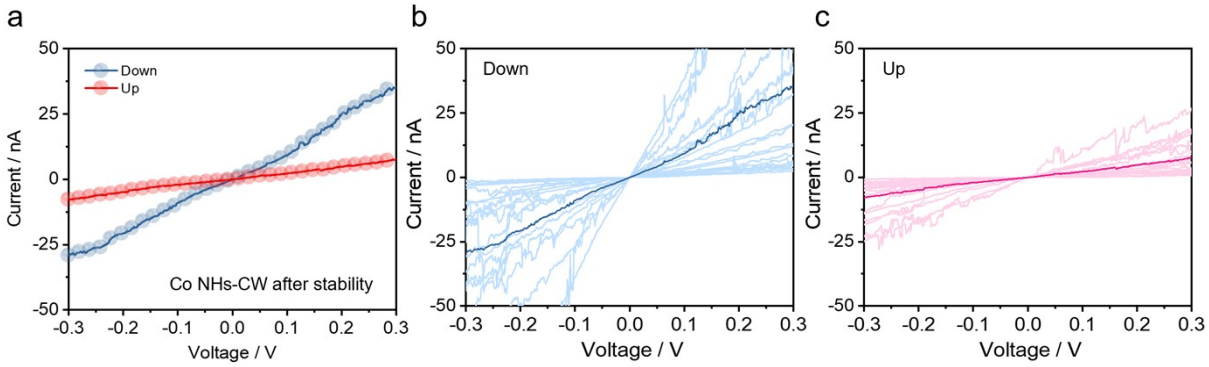

Fig. S27 a) Average results and b),c) raw data for $I-V$ curves obtained from mCP-AFM measurements with a pre-magnetized tip aligned along the upward or downward magnetic field orientations at different positions on Co NHs-CW after stability test.

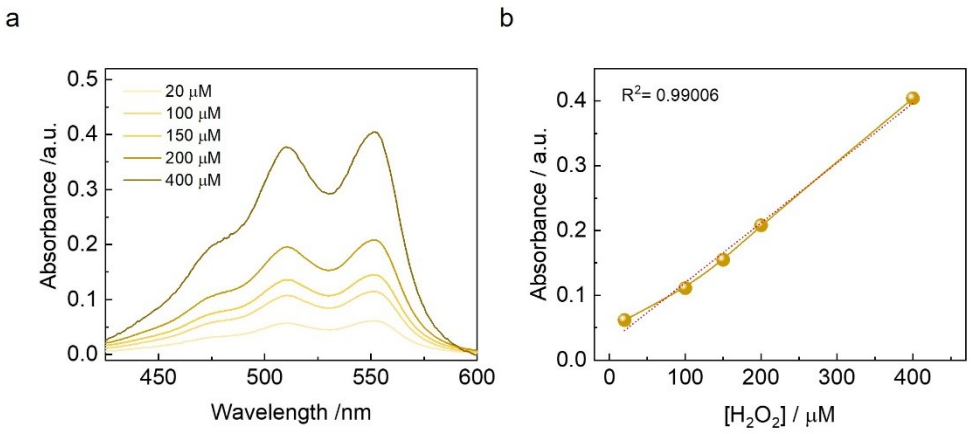

Fig. S28 a) Absorbance spectra for different (known) contents of H_2O_2. A calibration curve was obtained based on the absorbance at 551 nm, using the colorimetric method. b) Resulting calibration curve as a function of H_2O_2 content.

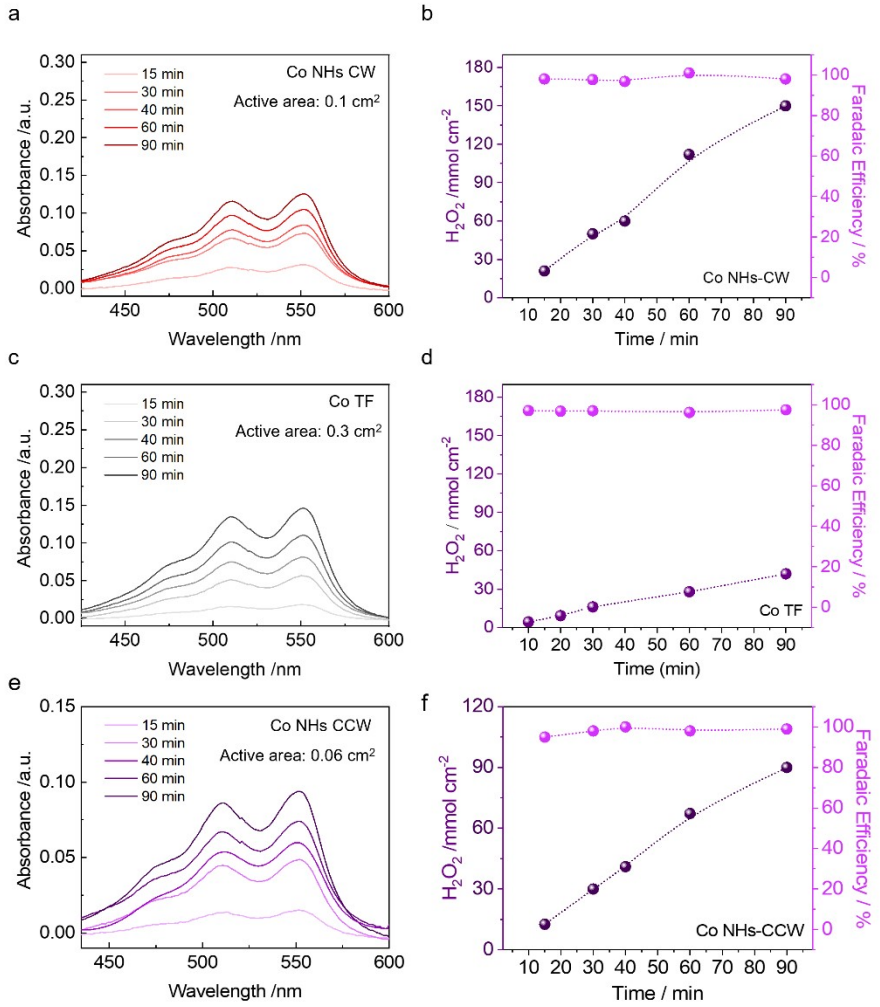

Fig. S29 Time-dependent absorption spectra of electrolyte aliquot as a function of reaction time for a) Co NHs-CW, c) Co TF, and e) Co NHs-CCW. Faradaic efficiencies of b) Co NHs-CW, d) Co TF, and f) Co NHs-CCW.

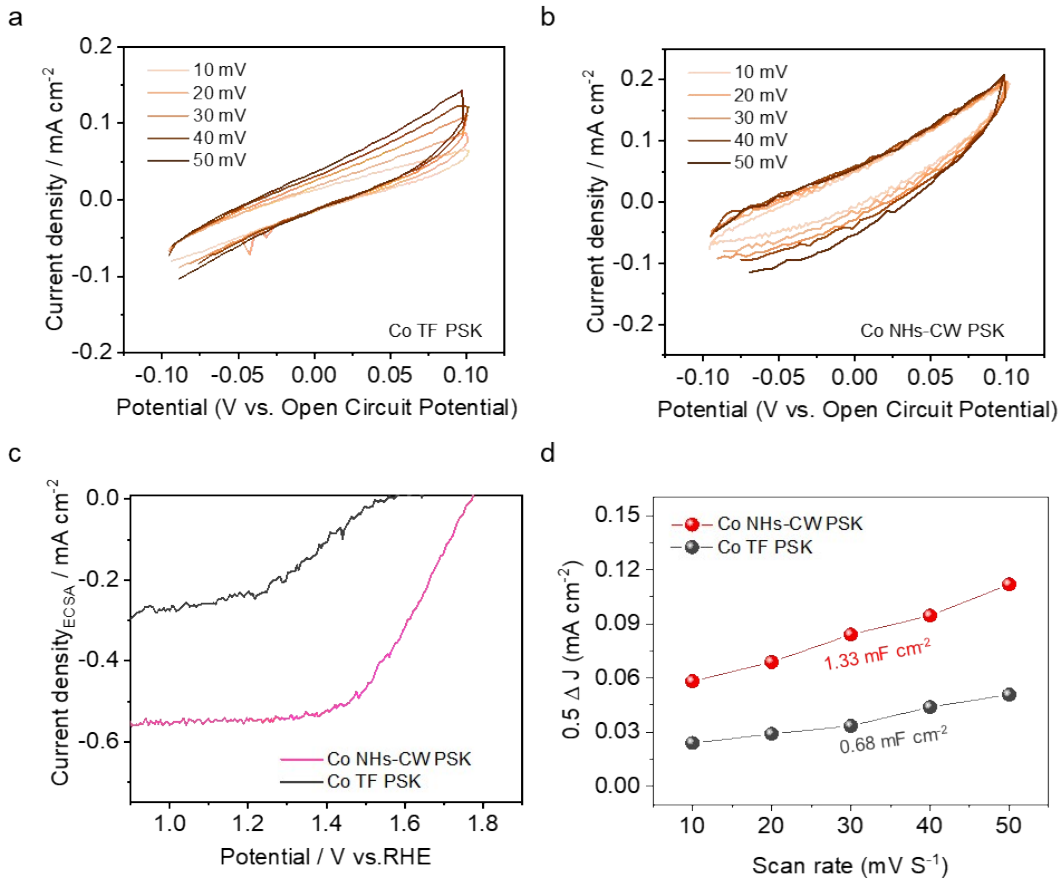

Fig. S30 CV curves for a) Co NHs-CW PSK and b) Co TF PSK in O_2-saturated 0.1 M KOH under 1-sun illumination. c) Capacitive current densities of Co NHs-CW PSK and Co TF PSK as a function of scan rate. d) LSV curves for Co NHs-CW PSK and Co TF PSK in O_2-saturated 0.1 M KOH under 1-sun illumination, based on ECSA-normalized current density.

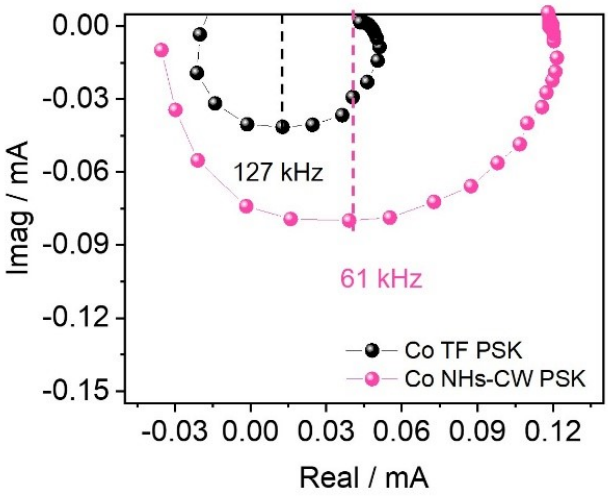

Fig. S31 Nyquist plots of IMPS spectra for Co NHs-CW PSK and Co TF PSK at 1.1 V_{RHE} in O_2-saturated 0.1 M KOH.

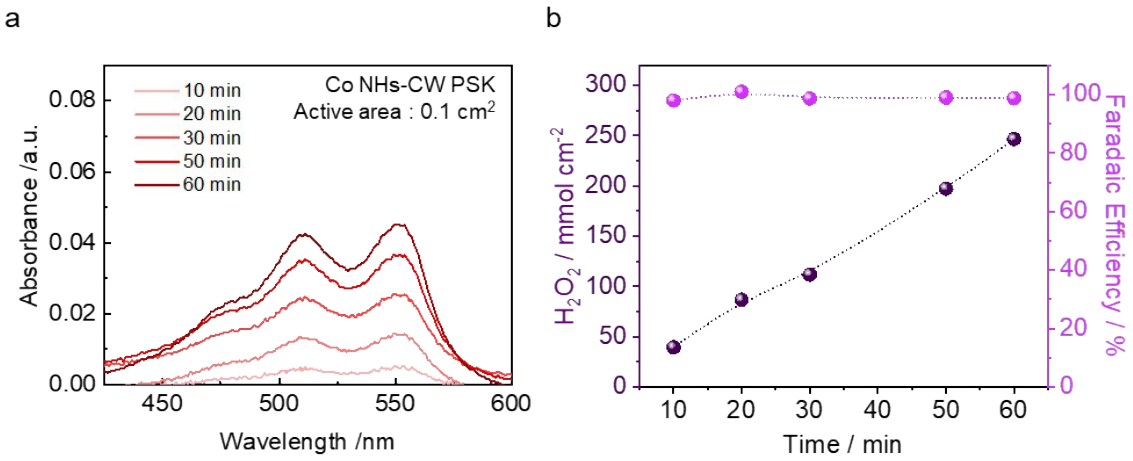

Fig. S32 a) Time-dependent absorption spectra of electrolyte aliquot as a function of reaction time for Co NHs-CW PSK. b) Faradaic efficiency of Co NHs-CW PSK.

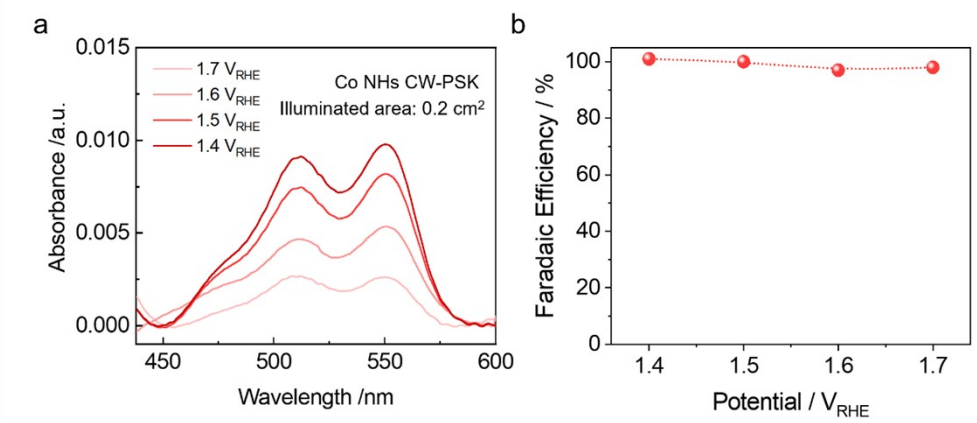

Fig. S33 a) Potential-dependent absorption spectra of the electrolyte aliquot as a function of potential and b) Faradaic efficiency for Co NHs-CW-PSK.

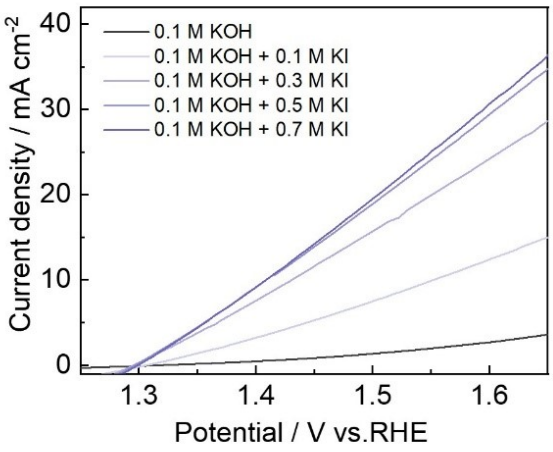

Fig. S34 LSV curves for carbon cloth electrode in 0.1 M KOH electrolyte with varying concentrations of KI.

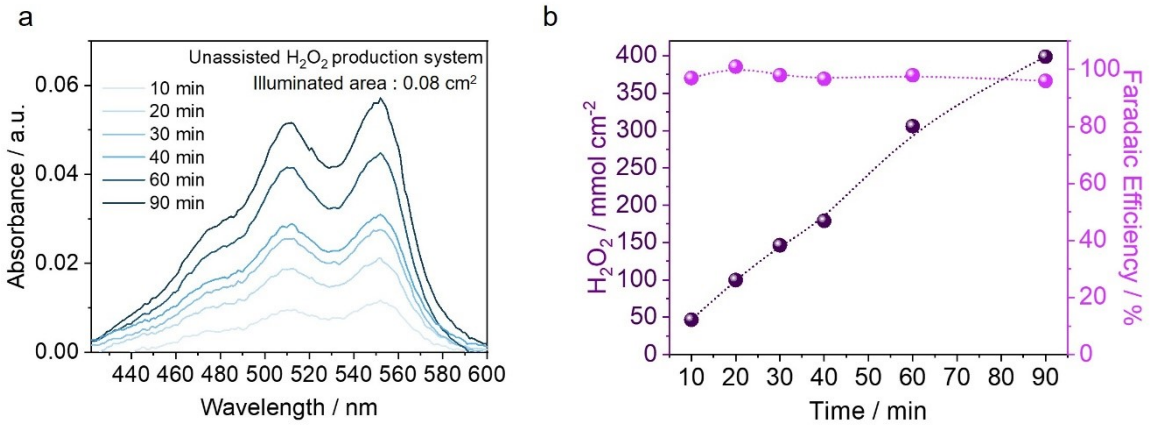

Fig. S35 a) Time-dependent absorption spectra of electrolyte aliquot as a function of reaction time for unassisted H_2O_2 production system. b) Faradaic efficiency of unassisted H_2O_2 production system.

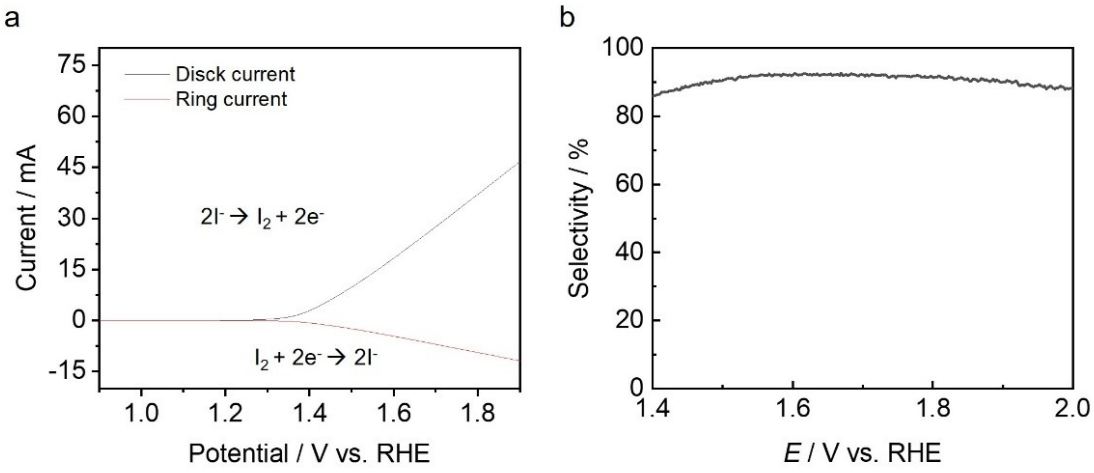

Fig. S36 a) Plots of disk current derived from graphite powders and ring current induced by Pt ring electrode in 0.1 M KOH + 0.5 M KI. b) Faradaic efficiency of IOR driven by graphite powders, based on RRDE analysis.

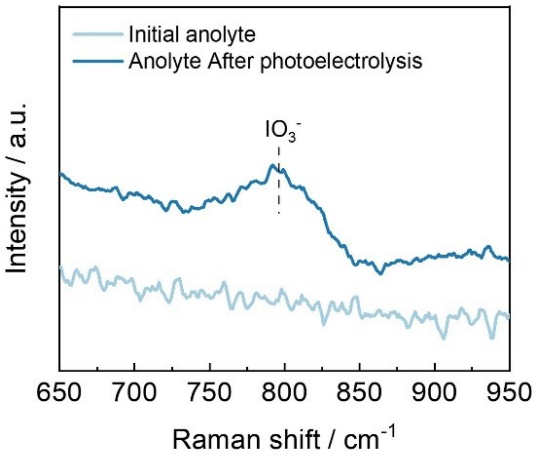

Fig. S37 Liquid Raman spectrum of final product of IOR in anolyte after photoelectrolysis driven by unbiased H_2O_2 production device.

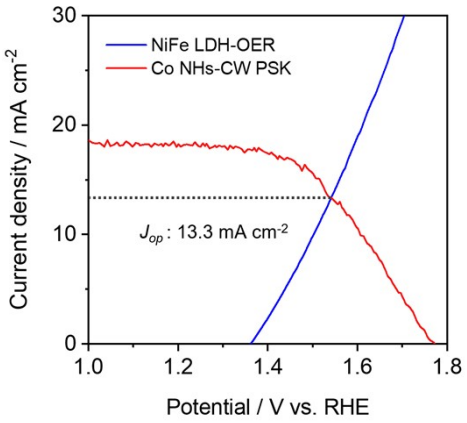

Fig. S38 LSV curves for Co NHs-CW PSK and NiFe LDH OER catalyst electrodes driving the 2e$^-$ ORR and OER processes, respectively.

Supplementary Table S1. Fitted impedance data of Co NHs-CW PSK and Co TF PSK.

Co NHs-CW PSK	R_s / Ω·cm^2	R_{ct} / Ω·cm^2
1.0 V_{RHE}	2.76	30.42
1.1 V_{RHE}	2.75	34.13
1.2 V_{RHE}	2.73	45.06
1.3 V_{RHE}	2.75	56.90

Co TF PSK	R_s / Ω·cm^2	R_{ct} / Ω·cm^2
1.0 V_{RHE}	1.81	91.22
1.1 V_{RHE}	1.84	102.40
1.2 V_{RHE}	1.86	119.62
1.3 V_{RHE}	1.82	139.37

Supplementary Table S2. Comparison table of SCC efficiencies of the present bias-free H_2O_2 production system based on the ORR-IOR configuration with previously reported unbiased systems using the OER as the anodic reaction.

Year	Electrode component	Coupled system	Stability / h	FE / %	SCC / %	Ref.
2019	TiO_2 photoanode || cathode Co-N/CNT	ORR-OER	27.8 h	64%	0.2%	S1
2020	$NiFeO_x/BiVO_4$ photoanode || cathode PTTh	ORR-OER	14 h	90%	0.7%	S2
2020	P-Mo-$BiVO_4$ || AQ-CNT/C	ORR-OER	5 h	100%	0.1%	S3
2021	*a*-$NiFeO_x$ || O-BP/FM/PSK	ORR-OER	12 h	100%	1.46%	S4
2021	RuO_x/TNR || AQ/graphite	ORR-OER	100 h	90%	0.37%	S5
2022	$SnO_{2-x}/BiVO_4/WO_3$-PTFE@Mo-SACs/mrG-GDE	ORR-OER	1 h	80%	1.46%	S6
2022	CoPi/$BiVO_4$ || Co-N/CNT	ORR-OER	5 h	80%	0.64%	S7
2022	2m-LDH/Ni/eu@nfOP || Co-containing LDH	ORR-OER	4 h	90%	3.24%	S8
2023	Mg:Ta_3N_5 || Nafion || CC/CMK-3	ORR-OER	3 h	70%	2.33%	S9
2024	CBS-based photocathode || PSK-based anode	ORR-OER	10 h	90%	1.46%	S10
2025	**Co NHs-CW PSK || carbon cloth**	**ORR-IOR**	**20 h**	**97%**	**9.4%**	**This work**

Supplementary Table S3. Calculated zero-point energy(ZPE) and experimental entropy contributions (TS) at 300K for molecules and adsorbate. TS terms for gas-phase species were taken from literature.[S11] The free energy of liquid water (H_2O(l)) was referenced to that of water vapor at equilibrium partial pressure of 0.035 bar at 300K.

molecule/adsorbate	**ZPE (eV)**	**TS (eV)**
H_2	0.27	0.41
H_2O	0.56	0.67 (0.035 bar)
*O	0.08	-
*OH	0.35	-
*H	0.18	-
*OOH	0.44	-

Supporting Information References

[S1] Ko, M., Pham, L.T.M., Sa, Y.J., Woo, J., Nguyen, T.V.T., Kim, J.H., Oh, D., Sharma, P., Ryu, J., Shin, T.J., et al. *Nat., Commun.*, 2019, **10**, 5123.

[S2] Fan, W., Zhang, B., Wang, X., Ma, W., Li, D., Wang, Z., Dupuis, M., Shi, J., Liao, S., and Li, C. *Energy Environ. Sci.*, 2020, **13**, 238-245.

[S3] Kawashima, A.B., Martins, L.D., Rafee, S.A.A., Rudke, A.P., de Morais, M.V., and Martins, J.A. *Environ. Sci. Pollut. Res. Int.*, 2020, **27**, 35941-35951.

[S4] Mehrotra, R., Oh, D., and Jang, J.W. *Nat. Commun.*, 2021, **12**, 6644.

[S5] Jeon, T.H., Kim, B., Kim, C., Xia, C., Wang, H., Alvarez, P.J.J., and Choi, W. E*nergy Environ. Sci.*, 2021, **14**, 3110-3119.

[S6] Dong, C., Yang, Y., Hu, X., Cho, Y., Jang, G., Ao, Y., Wang, L., Shen, J., Park, J.H., and Zhang, K. *Nat. Commun.*, 2022, **13**, 4982.

[S7] Song, J., Yu, J.M., Ahn, J.H., Cho, H., Oh, J., Kim, Y.S., Kim, J., Ko, M., Lee, S.-h., Shin, T.J., et al. *Adv. Funct. Mater.*, 2022, **32**, 2110412.

[S8] Zhu, D., Feng, C., Fan, Z., Zhang, B., Luo, X., and Li, Y. *Sustainable Energy & Fuels*, 2023, **7**, 3326-3332.

[S9] Moon, S., Park, Y.S., Lee, H., Jeong, W., Kwon, E., Lee, J., Yun, J., Lee, S., Kim, J.H., Yu, S., and Moon, J. *Energy Environ. Sci.*, 2024, **17**, 5588-5600.

[S10] Ko, M., Kim, Y., Woo, J., Lee, B., Mehrotra, R., Sharma, P., Kim, J., Hwang, S.W., Jeong, H.Y., Lim, H., et al. *Nat. Catal.*, 2022, **5**, 37-44.

[S11] CRC Handbook of Chemistry and Physics, 93rd ed.; CRC Press: Boca Raton, FL, 2011−2012.